Chapter 2

DATA PRESENTATION

2.1 The Data

The data I used for the completion of this thesis project represents 44% of the LITTLE THINGS data (Hunter et al., 2012). The LITTLE THINGS (Local Irregular That Trace Luminosity Extremes, The H I in Nearby Galaxies Survey) project shifts the interest in objects like nearby spiral galaxies as it was for the THINGS project (Walter et al., 2008) to nearby, relatively normal, gas-rich dwarfs. The LITTLE THINGS Survey uses a multi–wavelength approach to investigate star formation in dwarf galaxies and shed some light on ~~very attractive topics like~~ what regulates star formation in small, gas rich galaxies, what is the importance of triggered star formation, what happens to star formation in the outskirts of galaxies, etc. The project combines young star tracers: Hα and *GALEX* ultraviolet images; old star tracers: *UBVJHK* and *Spitzer* 3.6 and 4.5 μm images; dust tracers: *Spitzer* PACS 5.8 and 8.0 μm images, IRS spectra of HII regions, and MIPS 24, 70 and 160 μm images of dust emission. To trace morphological and kinematical structures that are important in star formation, the multi–wavelength domain is completed with H I data. The H I furthermore provides crucial information on the kinematics of the gas.

The LITTLE THINGS sample is drawn from a larger sample of 94 dwarf irregulars, 24 BCDs (Blue Compact Objects) and 18 Sm galaxies, observations collected over a 15 years period and investigated at different wavelengths by Hunter & Elmegreen (2004, 2006). The LITTLE THINGS sample is composed of 41 dwarfs: 37 dwarf irregulars and 4 BCDs. The following subsections give details on how

the observations, data calibration, data combination and imaging were done for the LITTLE THINGS galaxies and implicitly for the 18 LITTLE THINGS dwarfs that are part of my thesis subsample.

2.1.1 Subsample Choice

The aim of this thesis is to study the star formation laws in extreme environments such as the ones in dwarf galaxies. To achieve this purpose the choice of which galaxies are part of the investigated subsample is not trivial. We guided our choice partly on the availability of ancillary data and mainly on sampling broadly three main dimensions of our parameter space: metallicity, luminosity and integrated star formation rates. In Table 2.1 is illustrated how our sample of 18 galaxies spans in metallicity (12+log(O/H)) from 7.2 for DDO 210 to 8.29 for DDO 168. We expect metallicity to play a very important role in our sample and influence the star formation mechanisms, therefore the subsample galaxies appear ordered by metallicity in all tables and plots. In terms of luminosity, the absolute V magnitude of the galaxies in our subsample ranges from -10.88 mag for DDO 210 to -17.63 mag for NGC4214. We immediately notice that lower metallicity doesn't necessarily mean lower luminosity, nor lower integrated star formation rate (SFR). The integrated SFR in our sample is based on FUV fluxes for all except two (DDO 155, DDO 165) galaxies, where FUV data were not available. The log of the integrated SFR ranges from -1.07 $M_\odot$ yr^{-1} kpc^{-2} for DDO 75 to -3.67 $M_\odot$ yr^{-1} kpc^{-2} for DDO 165, this latter value being based on the Hα flux.

The galaxies in our subsample are no further than 4.6 Mpc away (DDO 165) and no closer than 0.7 Mpc (IC 1613). Table 2.2 illustrates best the range of wavelengths, and consequently instruments, we used in our attempt to get as complete a picture as possible on what governs star formation in dwarf galaxies. The ancillary data and its origin is discussed in Section 2.1.2.

To ensure continuity between our study and previous studies in this field (e.g. Leroy et al., 2008; Bigiel et al., 2010b) and to ease the comparison of our results with the literature we, overlapped our sample with the THINGS sample. Therefore, seven of the THINGS galaxies (DDO 50, DDO 53, DDO 63, DDO 154, M81dwA, NGC 2366, NGC 4214), passed onto the LITTLE THINGS project have been chosen to be part of our subsample.

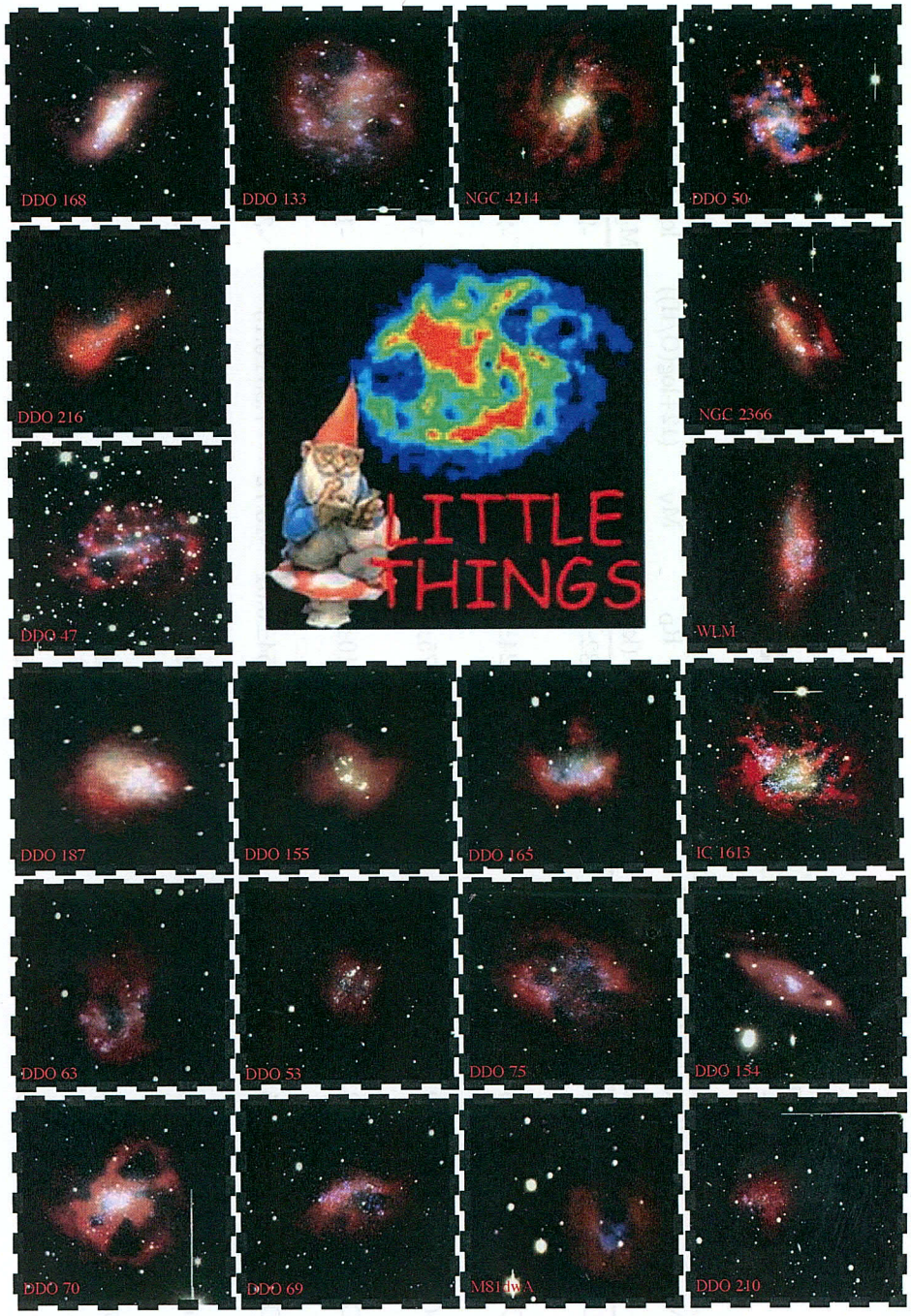

Figure 2.1: Composites of the H I map as red, FUV map as blue and V image as green for all galaxies in my thesis subsample (credit to Lauren Hill at Lowell Observatory for making them). North is at the top; east is to the left.

Table 2.1. General properties

Name	RA [J2000] (hh mm ss.s)	DEC [J2000] (dd mm ss.s)	D (Mpc)	R_H (′)	R_D (kpc)	M_V (mag)	(12+log(O/H))	log (SFR_D) ($M_\odot$ yr^{-1} kpc^{-2})
DDO 168	13 14 27.9	45 55 09.0	4.3	2.32	0.82±0.01	-15.27	8.29±0.07	-2.04±0.01
DDO 133	12 32 55.4	31 32 14.1	3.5	2.33	1.24±0.09	-16	8.23±0.09	-2.62±0.01
NGC 4214*	12 15 39.2	36 19 38	3.0	4.67	0.75±0.01	-17.63	8.17±0.06	-1.08±0.01
DDO 50*	08 19 08.7	70 43 25.0	3.4	3.97	1.10±0.05	-16.61	8.13±0.11	-1.55±0.01
DDO 216	23 28 35.0	14 44 30	1.1	4.00	0.54±0.01	-13.72	7.93±0.15	-3.21±0.01
NGC 2366*	07 28 48.8	69 12 22.0	3.4	4.72	1.36±0.04	-16.79	7.91±0.01	-1.66±0.01
WLM	00 01 59.2	-15 27 41	1.0	5.81	0.57±0.03	-14.39	7.83±0.06	-2.05±0.01
DDO 187	14 15 56.7	23 03 19	2.2	1.06	0.18±0.01	-12.68	7.69±0.09	-1.98±0.01
DDO 155	12 58 39.8	14 13 10.0	2.2	0.95	0.15±0.01	-12.53	7.68±0.06	-1.44±0.01**
DDO 165	13 06 25.3	67 42 25.0	4.6	2.14	2.26±0.08	-15.60	7.63±0.08	-3.67±0.01**

IC 1613	01 04 49.2	02 07 48	0.7	9.10	0.58±0.02	-14.60	7.62±0.05	-1.99±0.01
DDO 63*	09 40 30.4	71 11 02.0	3.9	2.17	0.68±0.01	-14.78	7.61±0.11	-1.95±0.00
DDO 53*	08 34 08.0	66 10 37.0	3.6	1.37	0.72±0.06	-13.84	7.60±0.11	-2.41±0.01
DDO 75	10 10 59.2	-04 41 56	1.3	3.09	0.22±0.01	-13.91	7.54±0.06	-1.07±0.01
DDO 154*	12 54 06.2	27 09 02	3.7	1.55	0.59±0.03	-14.19	7.54±0.09	-1.93±0.01
DDO 69	09 59 25.0	30 44 42.0	0.8	2.4	0.19±0.01	-11.67	7.38±0.10	-2.22±0.01
M81dwA*	08 23 57.2	71 01 51	3.6	...	0.26±0.00	-11.73	(7.3)	-2.26±0.01
DDO 210	20 46 52.0	-12 50 50.0	0.9	1.31	0.17±0.01	-10.88	(7.2)	-2.71±0.06

Table 2.1: From left to right the columns represent: Galaxy name, RA, DEC, Distance (see taken Hunter et al. (2012)), Holmberg radius measured to a B-band surface brightness of about 26.66 from Hunter & Elmegreen (2006),Disk scale length measured from V–band images R_D (Hunter & Elmegreen, 2006), Absolute V magnitude from Hunter & Elmegreen (2006), Metallicity from Hunter et al. (2012), SFR from Hunter et al. (2012) determined from GALEX FUV fluxes divided by πR_D^2. A double star next to the SFR value indicates a FUV flux was not measured and the SFR value is determined from $L_{H\alpha}$ divided by πR_D^2. A star next to the galaxy name indicates the galaxies that are shared between the LITTLE THINGS and the THINGS projects. The galaxies in this table are ordered by metallicity.

2.1.2 Ancillary Data

The UBV optical data of our subsample were obtained with five different telescopes: the 1.1–m Hall telescope at Lowell Observatory, the 1.8–m Perkins telescope, the Kitt Peak National Observatory 4–m telescope, the Schmidt telescope at Cerro Tololo Inter-American Observatory, and the 0.9–m telescope at Cerro Tololo Inter-American Observatory, from 1993 to 2002 (see Table 2.2). We have $K-$band observations available for only three galaxies in our subsample: DDO 168, NGC 4214, and NGC 2366. These were obtained from 1996 to 1998 again at Lowell Observatory with the 1.8–m Perkins telescope. More details on the instrumental setup and data processing can be found in Hunter & Elmegreen (2006), where these data have been published. The Hα data were observed from 1988 to 1998 in a large campaign dedicated to irregular galaxies. Details of that campaign and its results can be found in Hunter & Elmegreen (2004). In Table 2.2 we only list the telescope names used for the Hα observations of each galaxy in our subsample. Two members of our subsample M81dwA and DDO 210 show no emission in Hα.

The FUV images used in this thesis have been obtained by the Galaxy Evolution Explorer satellite (*GALEX*) which images simultaneously in two channels FUV (bandpass of 1350-1750 Å and resolution of 4″) and NUV (bandpass of 1750-2800 Å and resolution of 5”6). The *GALEX* data processing details and analysis is presented in Hunter et al. (2010). Out of the 18 dwarf galaxies members of our subsample, two DDO 155 and DDO 165 were not observed in FUV. The *Spitzer* data have been acquired as part of large surveys such as the SIRTF Nearby Galaxies Survey (SINGS; Kennicutt et al., 2003) and the Local Volume Legacy (LVL; Dale et al., 2009), which made available to the astronomical community significant libraries of data on nearby galaxies in a multitude of bands of which we use 3.6 μm and 24 μm.

Table 2.2. Ancillary Data Observation Settings

Name	Alt. Name	Optical Bands UBVJHK	Telescope (UBVJHK)	Instrument (FUV)	Instrument (3.6 μm, 24 μm)	Telescope (Hα)
DDO 168	PCG 46039	UBV	HT	*GALEX*	*Spitzer*	PT, FP, NCCD
	UGC 8320	JHK	PT			
DDO 133	PCG 41636	UBV	HT	*GALEX*	*Spitzer*	PT, FP, NCCD
	UGC 7698	J	PT			
NGC 4214	PCG 39225, UGC 7278	UBV	KPNO4m	*GALEX*	*Spitzer*	PT, 4:1, NOTI
	PCG 39225, UGC 7278	JHK	PT			
DDO 50	PCG 23324, UGC 4305	UBV	HT	*GALEX*	*Spitzer*	PT, 4:1, NOTI
	Holmberg II, VIIZw 223	...	...			
DDO 216	PGC 71538, UGC 12613	UBV	KPNO4m	*GALEX*	*Spitzer*	PT, 4:1, NOTI
	Peg DIG, Pegasus Dwarf	...	...			
NGC 2366	PGC 21102	UBV	KPNO4m	*GALEX*	*Spitzer*	PT, FP, NCCD
	UGC 3851, DDO 42	JHK	PT			
WLM	PGC 143, UGCA 444, DDO 221	UBV	HT	*GALEX*	*Spitzer*	PT, FP, NCCD
	Wolf-Lundmark-Melott	...	...			
DDO 187	PGC 50961	UBV	HT	*GALEX*	*Spitzer*	PT, FP, NCCD
	UGC 9128	J	PT			
DDO 155	PGC 44491, UGC 8091	UBV	HT	...	*Spitzer*	PT, 4:1, NCCD
	LSBC D646-07, GR 8	J	PT			
DDO 165	PGC 45372, UGC 8201	UBV	HT	...	*Spitzer*	PT, FP, NCCD

	IIZw 499, Mailyan 82	J	PT			
IC 1613	PGC 3844	UBV	CTIOs	*GALEX*	*Spitzer*	PT, FP, NCCD
	UGC 668, DDO 8	...	...			
DDO 63	PGC 27605, UGC 5139	UBV	HT	*GALEX*	*Spitzer*	HT, 2048
	Holmberg I , Mailyan 044	...	...			
DDO 53	PGC 24050	UBV	KPNO4m	*GALEX*	*Spitzer*	PT, FP, NCCD
	UGC 4459, VIIZw 238	JH	PT			
DDO 75	PGC 29653	UBV	CTIO0.9m	*GALEX*	*Spitzer*	PT, FP, NCCD
	UGCA 205, Sextans A	...	...			
DDO 154	PGC 43869, UGC 8024	UBV	HT	*GALEX*	*Spitzer*	PT, 4:1, NCCD
	NGC 4789A	...	...			
DDO 69	PCG 28868	UBV	HT	*GALEX*	*Spitzer*	PT, FP, NCCD
	UGC 5364, Leo A	...	...			
M81dwA	PGC 23521	UBV	HT	*GALEX*	*Spitzer*	HT, 2048
DDO 210	PGC 65367, Aquarius Dwarf	UBV	KPNO4m	*GALEX*	*Spitzer*	KPNO4m, Mos, HT, 2048

Table 2.2: From left to right the columns represent: Galaxy name, Other names, Optical bands observations, Instruments used for the optical bands observations, Instrument used for the FUV observations, Instrument used for the 3.6 μm, 24 μm observations , Instrument used for the Hα observations. The telescope codes are the following: HT= 1.1–m Hall telescope at Lowell Observatory, PT= 1.8–m diameter Perkins telescope at Lowell Observatory, FP= Ohio State University Fabry-Perot used as a simple 3:1 reducer, 4:1= 4:1 focal reducer, KPNO4m= Kitt Peak National Observatory 4–m telescope, Mos= KPNO mosaic camera, 2048= SITe 2048×2048 CCD, NCCD= a TI 800×800 CCD provided to the Lowel Observatory by the National Science Foundation, NOTI= a TI 800×800 CCD on loan to the Lowell Observatory from the US Naval Observatory, Flagstaff station, CTIOs= Schmidt telescope at Cerro Tololo Inter-American Observatory, CTIO0.9m= 0.9–m telescope at Cerro Tololo Inter-American Observatory. The galaxies in this table are ordered by metallicity.

2.2 H I Observing Strategy and Data reduction

With the ancillary data at hand, the LITTLE THINGS team was awarded 376 hours of observations with the Very large Array (VLA) to observe neutral hydrogen in a sample of 42 dwarfs. For all these galaxies we combined observations from the VLA archives where available with new observations where necessary in order to achieve complete sets of B–, C– and D–array data. Among these galaxies, DDO 216 is the only one for which observations in the B–array configuration were not performed. For the galaxies inherited from the THINGS project (DDO 50, DDO 53, DDO 63, DDO 154, M81dwA, NGC 4214, NGC 2366) we have used the THINGS' team calibrations and data combination and we have only changed the imaging technique, using the Multi–Scale CLEAN (see §2.3) instead of the residual rescaling imaging technique used by Walter et al. (2008). In my subsample of 18 galaxies, three data sets for the galaxies DDO 168, DDO 187 and DDO 155 are composed of completely new observations, the one on DDO 168 being discussed in detail in §3.

The new observations were scheduled while the VLA was going through its upgrade to EVLA: the old VLA front–end and back–ends being replaced with new EVLA ones. Until the new correlator came online, to continue functioning the telescope relied on hardware to convert the digital signals from the EVLA front–end into analog signals to be fed into the VLA correlator. This conversion however caused extra power to be aliased into the bottom 0.7 MHz of the baseband, being strongest at the lowest frequencies and dropping off rapidly with frequency. The aliased signal manifests itself on EVLA–EVLA baselines as a noise increase, the correlator power entering with a quasi–random phase, thus scattering this aliased signal across the map. On VLA–EVLA baselines the signals are largely uncorrelated, leading to only a marginal noise increase. As the upgrade progressed however, the number of EVLA–EVLA baselines increased, leaving fewer reliable baselines to work with.

2.2.1 Observing strategy

Signal being aliased into the first 0.7 MHz of the baseband has a serious impact on observing, especially when observing in narrow bands as it affects all fields that contain continuum emission. In spectral line mode the actual line emission may not suffer from aliasing if the bandwidth used is at least 1.5 MHz and the spectral line is narrow, falling beyond the affected 0.7 MHz. The phase and bandpass calibrators

are continuum sources, hence they are affected. In most cases, for the galaxies, the field of view will contain both line and continuum emission and removing the continuum requires extra care.

In all cases noise is aliased into the band and will decrease the effective sensitivity, with the channels closest to the baseband edge being the most affected. This is most noticeable on EVLA–EVLA baselines, and to a lesser extent on EVLA–VLA baselines; VLA–VLA baselines are not affected (see Fig. 2.2).

We observed without Doppler tracking, at a fixed frequency, to avoid phase jumps on EVLA–VLA baselines. We added a dummy scan to make sure the antennas start observing at the same time from the very start of our observing session. We selected our calibrators to be strong sources, to ease the calibration process and added extra calibrator scans bracketing the source whenever there was a need for a change in frequency, in order to track phase jumps due to the frequency changes.

In our observations we had a number of sources which were being observed through Galactic H I. The standard approach in these cases is observing both primary and secondary calibrators offset from the Galactic H I contaminated zone of the band. For our observations, however, we observed only the primary calibrator with a plus and minus offset, avoiding in this way further changes in frequency when looking at the secondary calibrator, changes that could easily cause compromising phase jumps.

To make up for the loss in sensitivity due to the aliasing problem, the VLA Telescope granted the LITTLE THINGS team extra observing time, which was dynamically scheduled, in small 2–3 hour blocks. Without an exact time allocation and without the Doppler tracking, the dynamically scheduled observations required careful planning to ensure that the observing frequency was the appropriate one for the aimed source at the time of observation. The sensitivity loss compensation came also at the price of more data reduction and more efforts in combining the different array data sets into a final one.

All new observations were made by us from late 2007 through to 2008. While the archival observations were done in 2IF mode with online Hanning smoothing and 128 channels, for the new observations, taken during the VLA to EVLA transition, we did not use online Hanning smoothing due to bandwidth considerations related to the special observing setup imposed by the EVLA–VLA transition. Any Hanning smoothing applied to the new data was done as part of the data reduction. For all the 18 galaxies in the subsample we have used as a flux density and bandpass calibrator one of the following three: 3C286, 3C48, 3C147. The choice of bandpass

calibrator (primary calibrator) was based on which of the three was on the sky at the moment of observation. The flux secondary calibrators, for each galaxy in our subsample are listed in Table 2.3. In general, the secondary calibrator was chosen on the basis of brightness and proximity to the source with all within about 12 degrees of the source. It was observed in scans of 4 minutes, alternating with every 20 minutes on source.

Table 2.3. Observation Settings

Name	Array Config.	Observing Date yy-mm-dd	TOS (min)	Secondary Calibrator	BW (MHz)	Han.	Chan. No.
DDO 168	D	08-Jul-07	120	1227+365	1.56	N	256
	C	08-Mar-27, 08-Apr-22	355	1227+365	1.56	N	256
	B	08-Jan-20, 08-Feb-01, 08-Feb-06	675	1313+549	1.56	N	256
DDO 133	D	04-Jun-21, 04-Aug-21/22	483	1221+282	1.56	Y	128
	C	08-Mar-22, 08-Jun-3	355	1227+365	1.56	N	256
	B	07-Dec-24, 08-Jan-11, 08-Feb-02	520	1227+365	1.56	N	256
NGC 4214*	D	94-Jan-27	135	1227+365	0.78	Y	128
	C	93-Aug-09	240	1227+365	0.78	Y	128
	B	94-Jun-30, 94-Jul-1	345	1227+365	0.781	Y	128
DDO 50*	D	91-Mar-07	105	0836+710	1.56	Y	128
	C	90-Dec-02	135	0836+710	1.56	Y	128
	B	90-Aug-10	330	0859+681	1.56	Y	128
DDO 216	D	08-Mar-22, Jun-3	122	2255+132	0.78	Y	128
	C	95-Mar-13	380	2255+132	0.78	Y	128
NGC 2366*	D	04-Jul-02	90	0614+607	1.56	Y	128
	C	04-Feb-23	120	0614+607	1.56	Y	128
	B	03-Dec-03	330	0614+607	1.56	Y	128
WLM	D	01-Oct-19	20	2321-163	1.56	Y	128
	C	00-Mar-31	312	2321-163	1.56	Y	128

	B	02-Jul-9, 02-Jul-12	504	2357-114	1.56	Y	128
DDO 187	D	08-Jul-11, 08-Aug-05, 08-Aug-06, 08-Aug-16	186	1330+251	1.56	Y	128
	C	08-Mar-28, 08-May-30	228	1330+251	1.56	Y	128
	CnB	08-Feb-10, 08-Feb-12	108	1330+251	1.56	Y	128
	B	07-Nov-17	474	1330+251	1.56	Y	128
DDO 155	D	08-Aug-17, 08-Aug-02	158	1347+122, 1254+116	0.78	N	256
	C	08-Jul-13, 08-Aug-02	300	1347+122	0.78	N	256
	B	07-Nov-17, 08-Feb-10	554	1254+116, 1347+122	0.78	N	256
DDO 165	D	08-Jul-06, 08-Jul-31	106	1313+675	1.56	N	256
	C	08-Mar-23, 08-Apr-14, 91-Jan-16	555	1313+675, 1358+624	1.56	N	256
	B	08-Jan-25 , 08-Feb-03, 08-Feb-09	540	1313+675	1.56	N	256
IC 1613	D	95-Apr-14	216	0106+013	1.56	Y	128
	C	96-Feb-11	354	0106+013	1.56	Y	128
	B	95-Dec-16, 95-Dec-18	726	0106+013	1.56	Y	128
DDO 63*	D	91-Mar-07	105	0836+710	1.56	Y	128
	C	90-Dec-02	135	0836+710	1.56	Y	128
	B	90-Jul-23	360	0917+624	1.56	Y	128
DDO 53*	D	04-Jul-09	90	0834+555	1.56	Y	128
	C	04-Feb-23	120	0834+555	1.56	Y	128
	B	03-Dec-22	360	0834+555	1.56	Y	128
DDO 75	D	92-Jul-13	90	0941-080	1.56	Y	128
	C	92-May-09, 04-May-14, 08-Mar-16	546	0941-080, 0943-083	1.56	Y	128
	B	05-May-09, 05-May-10, 07-Nov-21	306	0943-083	1.56	Y	128
	AB	94-Jun-17	42	0941-080	1.56	Y	128

DDO 154*	D	04-Jul-05	90	1330+251	1.56	Y	128
	C	04-Apr-28	150	1330+251	1.56	Y	128
	B	05-May-06	375	1330+251	1.56	Y	128
DDO 69	D	92-Jul-19	110	1003+351	0.78	N	256
	C	92-Apr-20 to Apr-21	250	1003+351	0.78	N	256
	B	95-Dec-02	420	1003+351	0.78	N	256
M81dwA*	D	01-Dec-10	195	0841+708	0.78	Y	128
	C	02-Nov-03	135	0841+708	0.78	Y	128
	B	03-Dec-16	345	0921+622	0.78	Y	128
DDO 210	D	02-Nov-01	186	2047-026	0.78	Y	128
	CD	95-Jan-20	122	2011-067	0.78	Y	128
	C	99-Jan-25	304	2011-067	0.78	Y	128
	B	02-Aug-02 , 02-Aug-09, 02-Aug-19	389	2011-067	0.78	Y	128

Table 2.3: From left to right the columns represent: Galaxy name, Array configuration, Observing Date, Time on source (TOS) in minutes, the secondary Calibrator, Bandwidth in MHz, Hanning smoothing: Y or N, and Number of Channels. A star next to the galaxy name indicates the galaxies that are shared between the LITTLE THINGS and the THINGS projects. The galaxies in this table are ordered by metallicity.

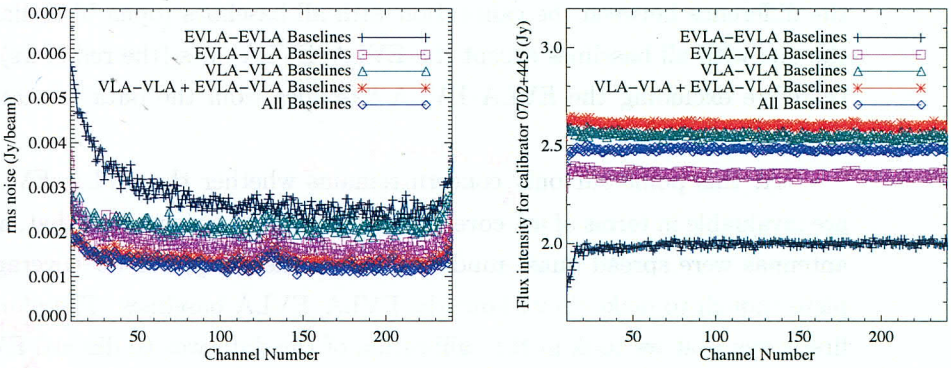

Figure 2.2: Noise level(left) and flux intensity of the secondary calibrator(right) as a function of channel number for data obtained observing with 26 antennas and 12 of them EVLA ones, during the EVLA–VLA transition period for different combination of baselines: all baselines (open blue diamonds), VLA–EVLA baselines (open magenta squares), VLA–VLA baselines (open green triangles), EVLA–EVLA baselines (navy plusses) and VLA–VLA plus VLA–EVLA baselines (red stars).

2.2.2 Data calibration and data combining

For the data calibration and reduction we used the AIPS package. Standard routines were used, although extra steps were necessary to deal with the problems brought on by the VLA upgrade. For a deeper understanding of the aliasing effect, we imaged separately different combinations of baselines and measured the noise in each channel of each resulting dataset, see Fig. 2.2. The navy plusses indicate the behaviour of the EVLA–EVLA baselines which are most affected by the aliasing effect,

In our tests, we have also found that due to the aliasing effect, the EVLA–EVLA baselines contribute to the overall dataset a considerable noise increase, so much so that the noise within the data set containing all baselines (blue open diamonds) and the noise within the data set without the EVLA–EVLA baselines (red stars) are at the same level. This means that even if it were possible to rescue the EVLA–EVLA baselines it would not improve the signal–to–noise level.

In the right panel of Fig. 2.2 we look at a secondary calibrator flux intensity as a function of channel number. In a properly calibrated data set we expect to see a flat line, around the value given for this particular calibrator in the calibrator's manual, which is 2.4 Jy. As a test we investigated how different combinations of baselines behave in this particular parameter space and we find that they are all flat and all lie within 0.2 Jy of each other in the same plot range except for the EVLA–EVLA baselines. This difference in flux level reflects the difference in bandpass between the old VLA and the new EVLA antennas. Once more we see that

the difference between the calibration with all baselines (open blue diamonds) and the one with all baselines except the EVLA–EVLA ones (the red stars) is minimal, therefore excluding the EVLA–EVLA baselines from the data set can only bring benefits.

At this point our only concern ~~remains~~ whether the EVLA–EVLA baselines are invaluable in terms of *uv*–coverage. After further tests we find that, as the EVLA antennas were spread quasi–randomly across the array, our *uv*–coverage was complete enough to make do without the EVLA–EVLA baselines. Therefore one of the first steps that we took in the calibration of the data was to discard EVLA–EVLA baselines.

~~To avoid any redundancies in the next paragraphs~~ we will present the data reduction and combining recipes used for our data by mentioning only the most outstanding steps taken to obtain high quality data and to attenuate the effects of the above mentioned observing setup difficulties. When loading data into AIPS, with FILLM, we allow channel/IF dependent weights and by doing so we get the true weight of all visibilities just as observed. The true weights represent valuable and accurate information on the IFs and antenna performance at the time of observation and when properly used can increase the sensitivity of the final image.

Once the data are loaded into the AIPS package, we remove 8% of the channels, 4% on each side of the band, using UVCOP. We choose to discard them at the very beginning because the noise affects the bandpass calibration, which is one of the first issues to deal with during the calibration. We run task SETJY to calculate the flux density of the primary calibrators. After removing the EVLA–EVLA baselines, flagging of other bad data, and correcting for the position of the antennas with VLANT we proceed with the bandpass calibration (the correction for channel to channel variations), using task BPASS, which removes VLA–EVLA closure errors due to non–matched bandpass shapes between VLA and EVLA antennas.

By correcting the bandpass, we can then proceed to reconstruct the Channel 0 using AVSPEC. It is this Channel 0 that we then further calibrate in a fairly standard manner. We copy over the FG table, a table containing all the bad data points and baselines, from the line data (uv visibilities as a function of all channels) to the new Channel 0 and execute task CALIB, which generates the SN table containing the complex gain solutions. Next GETJY calculates the flux density of the secondary calibrator and sets the SN table amplitude gains to reflect a common flux density scale. CLCAL creates from the SN table through interpolation a new version of the CL table, containing the complex gain corrections at all time inter-

vals, which applied to the data complete the calibration process. We then check our calibrated Channel 0 in TVFLG, and image the data. We then transferred the SN table from the CH0 to the line data and ran CLCAL on the line data.

At crucial points in our calibration recipe we run a number of tests to check the quality of the calibration to detect any possible problems. These tests involve checking the weights of the data using ANBPL, checking the amplitudes and phases versus *uv*–distance with UVPLT for calibrators and the target, checking vector averages of all data for each calibrator and the target with POSSM, making dirty images of the secondary calibrator and the source from the calibrated new channel 0, as well as making dirty cubes of the galaxy at the end of the line calibration.

For the LITTLE THINGS galaxies we have radio interferometric data for all galaxies in three different arrays B, C and D that are combined into one dataset. Some of the data in the LITTLE THINGS sample is from the archive, while the rest is recently observed. The archival data, such as the D array data on DDO 133, are Hanning smoothed while the new data is not. Once calibrated, we run CVEL to correct the frequencies from scan to scan as well as to align the dynamically scheduled observations with the regular ones. If Hanning smoothing is necessary, it can be applied to the data within CVEL. Although CVEL applies the Hanning smoothing, it does not get rid of every other channel, which is what was done with the archival data; for that we use task UVDEC. Once the data sets have the same frequency resolution and sampling, are aligned in velocity and precessed to the same J2000 epoch we use task DBCON to merge them into the final dataset. Because we opted not to use the EVLA–EVLA baselines, the continuum subtraction becomes a matter of simply linear fitting using the channels without emission on both sides of the line profile. We use UVLSF, and a linear baseline, to extract the continuum based on the location of channels free from line emission identified in a dirty cube of all data combined. Once the data is combined and continuum subtracted, we make a standard IMAGR map to check for calibration and array combination errors. Continuum maps were also created.

2.3 Imaging

In the radio domain, to achieve higher angular resolution, we make use of interferometers, which measure the Fourier transform of the sky intensity distribution. However, interferometric data is affected by incomplete coverage of the

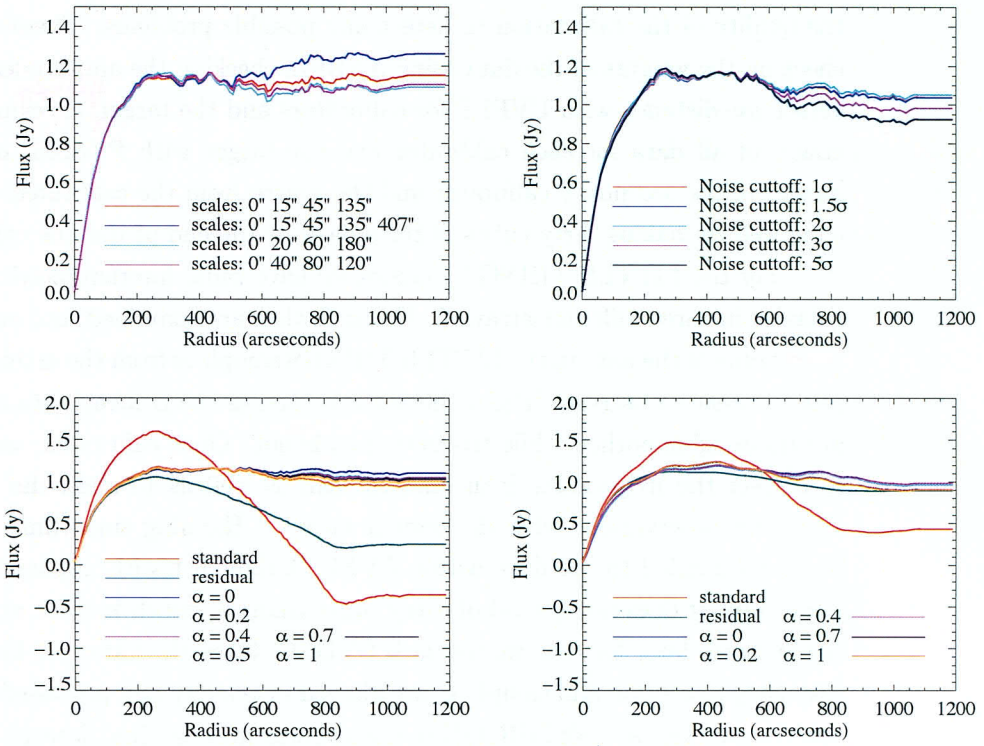

Figure 2.3: Top Left: Integrated Flux density vs radius in DDO 168; with α =0.2, robust=0, different combinations of scales (red: 0 15 45 135, green: 0 15 45 135 407, blue: 0 20 60 180, magenta: 0 40 80 120). Top Right: Flux vs radius in DDO 168; with α =0.2, robust =0, variable flux cut–off (red: 1σ , green: 1.5σ , blue: 2σ, magenta: 3σ, cyan: 5σ). Bottom Left: Flux vs radius in DDO 168; cleaned to 2σ level, robust 0, α parameter variable (red: standard CLEAN, green: residuals scaled standard CLEAN, blue: $\alpha = 0$, magenta: $\alpha = 0.2$, navy blue: $\alpha = 0.4$, cyan: $\alpha = 0.5$, orange: $\alpha = 0.7$, yellow: $\alpha = 1$). Bottom Right : Flux vs radius in DDO 168; cleaned to 2σ level, natural weighting, α parameter variable (red: standard CLEAN, green: residuals scaled standard CLEAN, blue: $\alpha = 0$, magenta: $\alpha = 0.2$, cyan: $\alpha = 0.4$, orange: $\alpha = 0.7$, yellow: $\alpha = 1$) .

but in captin the take away parts.

aperture plane: unmeasured short–baseline information, missing baselines, missing or deleted hour angle ranges. To remove these effects, deconvolution algorithms are needed and so the CLEAN method (Högbom, 1974) was developed.

In order to improve the quality of our maps we have invested effort in understanding which are the shortcomings of using CLEAN for low signal to noise extended sources such as the dwarfs galaxies. The disadvantages of CLEAN are:

- In cases of low signal to noise, CLEAN may start to find delta functions in places where only noise spikes are present. (Solution: For sources of known structure, windowing to limit the area of delta functions search speeds up the algorithm and makes it more reliable. Normally the flux of a clean component is set to 10% of the peak flux of the residual map, percentage also known as a loop gain. Lowering the value of the loop gain is also a solution to the above mentioned problem, however, it increases the computation time by requiring a greater number of delta functions).

- In case of extended sources, the contribution to the integrated flux from an extended, low-level intensity distribution can be substantial, even if the brightness in each pixel is below the noise level, which means that CLEAN has to go to very low levels to recover all signal. However, it is very difficult to do so, as CLEAN diverges when reaching levels of less than a sigma. (Solution: Smoothing the map to a lower resolution improves the signal to noise ratio per pixel for extended sources, however, it also loses information on the small scale structure, the very information one was trying to obtain by means of attaining higher angular resolution).

- For extended sources, the diameter of the source should not exceed the radius of the first grating response, otherwise CLEAN cannot reliably deconvolve.

- When the synthesized beam has strong side-lobes, CLEAN can introduce corrugation, parallel stripes in the clean map. These stripes are artificially created, when delta functions are found at the position of spurious peaks resulting from side-lobes of a dirty beam subtracted at a nearby position. Such a map will be consistent with the data, but it will not be a realistic brightness distribution

(Schwarz, 1984).

- CLEAN is in difficulty when trying to deal with missing short spacing for extended sources, because in their case a large part of the signal is in the short baselines and only a small part of the Fourier Transform is sampled. Another effect of the missing short spacings is the variation of the zero level, also known as the negative bowl. If we consider a source with a box-like intensity, its FT will be a sinc2 function. The centre part, however, is missing from the observation; in the map the central part of the sinc2 function is subtracted resulting in a large depression. (Solution: Obtaining single dish data to fill in the short spacings void while a useful solution, is not a trivial one, since it involves combining radio data from very different instruments.)

Since the 1980s, as the the above mentioned disadvantages became clearer different attempts have been made to improve CLEAN, either by using practical solutions such as windowing or a different loop gain, in combination with CLEAN, either by looking into alternatives to the CLEAN method itself. Historically speaking, here are some of the alternatives to CLEAN that have been proposed over the years:

- **Cornwell (1983)** modifies CLEAN by adding a delta function to the beam, an improvement not suitable to very extended sources.

- **Braun & Walterbos (1985)** provides a way to extrapolate the data in the uv plane, however this method is not able to remove the side-lobes.

- **Steer et al. (1984)** define a component as an area in which the intensities are above a certain cut–off and convolve the data in that area with the beam.

- **Brinks & Shane (1984)** suggest a way to use CLEAN to deconvolve a smooth dirty map and still keep the original resolution; they call it multi-resolution clean. This method has the disadvantage that it first finds the clean components at the highest scale, subtracts them and then moves down to the lower scales and by doing so it contaminates the lower scales with artefacts

created when smoothing the holes produced when cleaning the high scale.

- **Wakker & Schwarz (1988)** follow onto the concept of multi-resolution clean and add to it without changing its name. The new multi-resolution clean does not modify the basic CLEAN but instead separates the process into several steps, each step a simple clean with optimised parameters. It creates two intermediary maps, the smoothed map, which has the advantage of making extended structures more point like and the difference map, obtained by subtracting the smoothed map from the original data, which if also cleaned, makes it possible to retain the original resolution. The disadvantage of this method is that the algorithm works sequentially on all considered scales, which might cause errors on selecting a scale size to be frozen in.

Whereas CLEAN deconvolution normally works by modelling the image as a collection of point sources and if is optimised for sources which are not extended compared to the size of the synthesised beam, Multi–Resolution CLEAN uses smoothing of the map and the dirty beam to decrease the number of delta functions and to go to lower levels (Wakker & Schwarz, 1988). A standard CLEAN map consists of a sum of two maps: one containing the restored clean components and the other containing the residual map. Usually the fluxes are determined on the combined map assuming that the clean beam is the correct one for the entire map, an assumption which fails on extended structures (Jörsäter & van Moorsel, 1995). In reality the flux is calculated correctly only for the cleaned part of the map, for the residual map it is overestimated by a factor equal to the ratio between the dirty and clean beam (for more details, see Walter et al., 2008). For this reason, a standard IMAGR cleaned image for extended structure can overestimate the flux by as much as 50% as shown in Fig. 2.3, bottom left panel, where the red line represents the flux versus radius for a standard IMAGR data cube. The THINGS project dealt with this effect by working with two sets of cubes, one with rescaled fluxes, represented in green in Fig. 2.3, bottom left panel, which contain the correct fluxes and one without rescaling which preserves the original noise characteristics (Walter et al., 2008).

Whereas the rescaling deals with overestimating flux, it does not deal with the intrinsic difficulty CLEAN has in dealing with missing short spacings. This is evident from Fig. 2.3 (bottom left panel), where one sees that the flux recovered by standard CLEAN (red line) gradually drops from 200″ to 800″ radius, reflecting a

large scale depression in this radius range and beyond. The extended, low–level intensity distribution is a major contributor to the integrated flux of extended sources, even if the brightness in each pixel is at low S/N, which means that CLEAN has to go to very low levels to recover all signal. It is very difficult to do so, as CLEAN tends to diverge when reaching levels below 1-2 σ. Also, in regions of low signal–to–noise, CLEAN may start to find flux in places where only noise spikes are present, a problem which can be ~~steered~~ contained to an extent by appropriate windowing.

To address the difficulties that the CLEAN algorithm has with extended emission, Wakker & Schwarz (1988) developed an algorithm, that solves sequentially, in the image plane, for point components and set size Gaussians. The idea of recovering an object by modelling it as a composition of various different scale sizes, rather than a collection of points has opened up a new direction in the field of imaging techniques: the Multi–Scale methods. These methods differ in the way the reconstruction algorithm ~~will be trying~~ tries to quantify the strength of the various contributing scales (Cornwell, 2008). The modern day Multi–Scale methods are:

- **Multi–Resolution Clean**: a special run of CLEAN, which emphasizes on the broad emission first and then finer and finer resolution. The dirty image and point spread function are smoothed and decimated to emphasize the broad emission. The resulted image is then used as an initial model for a CLEAN deconvolution of the full resolution image.

- **Multi–Scale Maximum Enthropy**: The image is reconstructed by estimating pixels in the combined space such that the convolution equation is satisfied, after setting a hierarchy of scale sizes. The performance of this algorithm can be improved by decomposing the image ~~to be estimated~~ into several channels of different resolutions (Starck et al., 2002). The disadvantages of this method are the following: it cannot recover simultaneously both compact and extended sources, results depend on the background level, the entropy functions give poor results for negative structures embedded in the background, and spatial correlation in the images is not taken into account.

- **Wavelets**: This type of algorithm searches for clean components not in the dirty image but in the multi-resolution wavelet transform of the dirty image based on the dirty beam. When the signal presents localized features, such as singularities or edges, these features can no longer be well represented by

Fourier basis functions, which extend to the whole spatial domain. Other basis functions, such as wavelets are better suited for a wide range of signals. Wavelets provide an ideal way to incorporate noise modelling and regularization in the deconvolution methods (Slezak et al., 1990; Starck et al., 2002). Disadvantage: Wavelet Clean is only available for images which do not contain large-scale structures.

- **Pixons**: This method estimates the pixel strengths along with an associated scale size, iteratively decomposing the true image into a collection of locally best-fit kernels (usually Gaussians). The combination of strength and scale size, it was called a pixon. It has been reported to have very good performance, however is not applicable to synthesis observations, because the assumptions that the PSF is compact and that the noise is independent and additive, is not true for Fourier Synthesis (Pina & Puetter, 1993; Puetter, 1995).

- **Adaptative Scale Pixels (ASP)**: This algorithm estimates the best Asp (=a simple functional form defined by specifying the Amplitude, Location and Scale), at the location of the peak in the residual image at each iteration. While the pixon method exploits the locality of the effects of the PSF to limit the dimensionality of the search space, MS-Clean explicitly limits the dimensionality of the space by decomposing the image into a fixed set of scales. Both the mentioned methods work with a fixed set which remains unchanged from iteration to iteration and does not admit any other scales than those in the fixed set. ASP does not impose a fixed set, but allows changes at each iteration. Due to the inherent coupling of pixels in the true image as well as due to the extent of the PSF, only a sub-set of Aspen change significantly at each iteration, sub-set which is referred to as an active-set and is to be determined at each iteration. Since the members of the sub-set are determined on the fly, the set of scales used at each iteration potentially changes from iteration to iteration as well as all possible scales admissible (Bhatnagar & Cornwell, 2004). Disadvantage: Although it is known to have a good deconvolution performance, it is computationally very expensive.

From the methods mentioned above only the Multi–Resolution CLEAN category can be applied to our data. In this category fall extensions of the Wakker and Schwarz algorithm, which have been implemented independently in CASA by Tim Cornwell (Multi–Scale CLEAN (Cornwell et al., 1999; Cornwell, 2008) and in AIPS by Eric Greisen (Multi–resolution CLEAN (Greisen et al., 2009). The advances in computing made it possible to solve for different size components simultaneously. Both the AIPS and CASA implementations belong to the Multi–Scale methods category, one of the main differences between them being that, whereas the CASA implementation operates in the map plane, the AIPS implementation subtracts the clean components in the *uv*–plane and re–images at each major cycle (Rich et al., 2008). To obtain our final data cubes we opt for the Multi–Resolution CLEAN (Greisen et al., 2009) within IMAGR in AIPS. From here on, although referring to the AIPS implementation, we will use the term of Multi–Scale CLEAN, showing in this way its affiliation to the Multi–Scale methods.

Multi–Scale CLEAN deals with extended structure by using, *a priori* knowledge of the strengths and weaknesses of the CLEAN algorithm and the advantages of smoothing. CLEAN is optimised for sources less extended compared to the size of the synthesised beam. At the same time, when smoothing, the ratio of the source size to beam size improves which means that what was extended in the original resolution is small scale in a smoothed map. More than that, the signal to noise in a smoothed map improves as well as long as the structure in the map remains resolved, allowing a much deeper clean and therefore ensuring that most of the flux is recovered. However, if one were to clean only the smoothed map than that will result in loss of interesting information on small scale structure. To ensure that information on all scales is retrieved, in the AIPS implementation of Multi–Scale CLEAN, the user can choose the model components to be used by specifying the number (up to a maximum of 10) and the widths of circular Gaussians that converted into tapers will be used to make beam and data images at each scale. The 0th scale ensures the recovery of small scale structure as well as deals with unresolved objects.

To implement the Multi–Scale CLEAN, AIPS uses the multi–facets approach available in IMAGR for wide–field imaging. As the sky is a sphere, approximating it to a two dimensional flat patch only holds for small enough patches of sky, called facets. In wide–field astronomy the imaging is done by imaging facets and putting them together in one image. While for the wide–field astronomer IMAGR is creating a final map as a composition of imaged adjacent facets, for the Multi–Scale CLEAN user IMAGR creates a map out of overlapping facets over the same area

of the sky, each facet representing a different resolution scale. At each major cycle, it selects one of the total number of facets (i.e. spatial scale), re–images that facet with the current residual uv data, finds clean components for that facet using minor cycles, subtracts those components from the data and continues until it reaches one of the stopping criteria, prompting clean to go through the next major cycle. The selection of which resolution should be cleaned is done by establishing which resolution has the highest peak flux. The algorithm stops when the flux level in all facets is below the user–defined flux cut–offs. Then, the clean components for all resolutions, each with their corresponding clean beam are restored to the image made at the finest resolution (Greisen et al., 2009). In more recent versions of AIPS (31DEC10 and 31DEC11) the clean components are restored to all facets resulting in cleaned maps for each resolution considered. In this way the AIPS implementation of the Multi–Scale CLEAN, works in both the image plane during the minor cycles and uv plane during the major cycles.

It should be stressed that the parameter choice ~~should~~ must be carefully tuned to the data set to be imaged. The Multi–Scale algorithm ~~is available~~ includes under the IMAGR task in AIPS ~~through~~ a number of steering parameters. The first two of them are NGAUS and WGAUS representing the number of scales to clean simultaneously and the approximate width of the scales used, in arcseconds. In the literature the AIPS Multi–Scale clean has been mainly applied to data sets from a single array configuration and for those 3-4 gaussians out of 10 possible have been used. We apply the algorithm to a B–, C–, and D– configurations combined data set and after several tests (see Fig. 2.3, top left panel) we decided on four gaussians of widths 0″, 15″, 45″, 135″.

Another important steering parameter is FGAUS which allows the user to impose a stopping criterion for each resolution. For our tests, we established our rms noise threshold by measuring the noise in each of the four resolutions (fields) of a dirty, line–free channel, imaged with Multi–Scale CLEAN. Consequently, we have four different noise levels to work with, one for each field. The four cut–off levels to be set in FGAUS are not independent being different smoothed versions of the same dataset (see Schwarz 1988).

We tested the FGAUS parameter, by setting different flux cut–offs: we tried deeper cleaning, down to 1σ and 1.5σ and more superficial cleaning to 3σ and 5σ. We plotted the integrated flux as a function of radius (see Fig. 2.3, top right panel), in order to understand how the cut–off cleaning level affects the recovering of all emission and to find the optimum cut–off level. It should be high enough, for

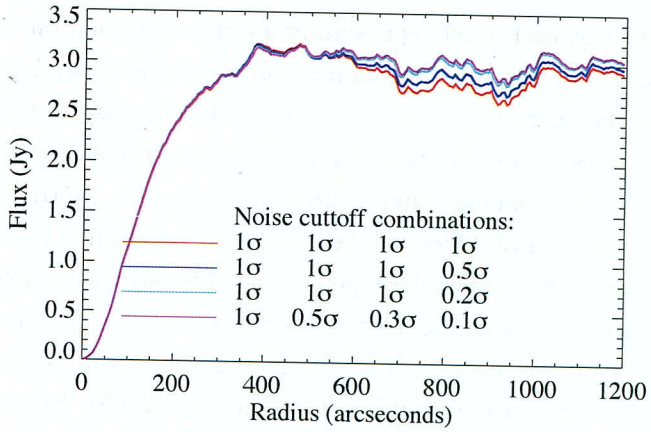

Figure 2.4: Integrated Flux density vs radius in DDO 168 for different noise cut–off combinations (red: 1σ in all four fields; blue: 1σ in field 1(highest resolution), 1σ in field 2, 1σ in field 3, 0.5σ in field 4(lowest resolution); cyan: 1σ in field 1(highest resolution), 1σ in field 2, 1σ in field 3, 0.2σ in field 4(lowest resolution); magenta: 1σ in field 1(highest resolution), 0.5σ in field 2, 0.3σ in field 3, 0.1σ in field 4(lowest resolution)).

Multi–Scale CLEAN not to diverge but it has to be low enough to retrieve the entire flux. Generally, problems arise when the extended nature of the source has it so that large visibility amplitudes are in the exact region, around the origin of the uv–plane, where the interferometer cannot probe. This problem, known as the "missing short spacings" reflects itself in the map plane through the presence of negative intensity regions or depressions, in the areas where the large scale structure has been filtered out by the instrument and around regions with positive flux. Deconvolution algorithms such as standard CLEAN have trouble dealing with negative flux areas at large radii. With Multi–Scale CLEAN we find that cleaning down to 3 or 5σ is not sufficient; because we are not retrieving all the flux, there remains a small depression at large radii. Cleaning down to 1, 1.5 or 2σ shows a levelling of integrated flux density at larger radii. Cleaning down to 1 or 1.5σ does not retrieve more flux than cleaning down to 2σ; however, clean artefacts such as holes start to become obvious in the final map. This actually means that we do not need to go any deeper than 2σ to retrieve the entire flux. Therefore for our LITTLE THINGS dwarf galaxies we are using as cut–off levels 2σ for the robust weighted cubes and 2.5σ for the natural weighted cubes. On the same idea we have also tested how changing the cleaning cut–off level in each field improves the imaging process (see Fig. 2.4). We found that the changes are minimal, however, cleaning to a lower cut–off level in the

lowest resolution than in the highest resolution field results in a flatter behaviour at large radii. It is important to note that such a per field differential cleaning implies knowing your source well enough to predict what the cut–off level should be in each field and most likely will be galaxy dependent.

Lastly, there is a steering parameter, IMAGRPRM(11). Naively one would look for the peak residual at any resolution, and choose the next clean component. However, in this way, since the lowest resolution always shows more flux as the beam area is larger, the algorithm will be biased towards the largest scales (Greisen et al., 2009).

Biasing towards or against a certain size structure is done by weighting the peak fluxes in each field by a factor of $1/[((\text{field beam area})/(\text{minimum beam area}))^{\text{IMAGRPRM(11)}}]$; in other words by controlling the IMAGRPRM(11) parameter, hereafter called the α parameter. This parameter gives one control over which resolution is going to be chosen next. If α=0, then the peak fluxes at each resolution are seen for what they are, hence the natural bias towards the largest scale as explained above becomes obvious. If α=1, the peak flux at the highest resolution will be the true peak flux, while the peak flux at all the other resolutions will be adjusted to its smallest value, which is a factor of the current beam over the highest beam, smaller than the true peak flux at that resolution. Thus, the highest resolution will be selected first and then all the others successively. To further understand how the biasing works we plot the choice of resolution in each major cycle when cleaning one channel with the AIPS Multi–Scale CLEAN (Fig. 2.5). This plot tells us how the α parameter influences the choice of cleaning resolution scale and the time spent cleaning with that particular resolution scale.

A balance between small and large scale structure components needs to be found, a balance that is dependant on the kind of object to be imaged. We have made tests on the appropriate choice of α and we find all different α maps have a very similar amount of total flux, which means that no matter which α one chooses, the algorithm is able to converge. Still, choosing the α parameter is in no way trivial. If we subtract too many small scale components (α =1), we will create holes which will be taken by the larger scales as real emission and converted to cleaned flux. On the other hand, if we clean too many components on the largest scale (α =0), we start converting noise to clean flux density and the algorithm may even diverge (see Fig. 2.3, bottom panels). In this same Figure, we can see that different α, although finding similar values in total flux, do behave differently at larger radii. When α=0, the algorithm finds the highest level of total flux (blue line). Most of the time the

α=0.2 line follows it very closely. In Fig. 2.3, however, at very large radii the difference between the α=0 line and the rest is more obvious probably because in the context of the particular structure of the object, DDO 168, having been biased towards using points as model components it starts interpreting smoothed noise as real emission and so increase artificially the overall flux found in the map. On the other hand, when α= 1 (yellow line), we are imposing IMAGR a model which says the source is very extended, so IMAGR will spend more time looking for extended components and what remains may not be picked up by the higher resolution within the clean cut–offs imposed. The α = 0.0, 0.2 and 0.4 flatten at large radii and are almost indistinguishable from one another.

The differences between 0.2 and 0.4 as choices for α become more evident when looking at the final and residual maps resulting from applying Multi–Scale CLEAN to a line emission channel for two different structured sources (see Fig. 2.7 and Fig. 2.8). If when looking at a source such as DDO 168 the differences between α= 0.2 and 0.4 are hard to distinguish, when looking at a more complicated source such as DDO 133 things become more obvious. While for α=0.2 the 15″, 45″ and 135″ residual fields look flat, for α=0.4 one can start seeing signs of over–cleaning (see Fig. 2.8). When comparing Fig. 2.7 and Fig. 2.8 one should also realise how much the choice of the α parameter actually depends on the complexity of the source to be imaged.

When investigating how different α values behave in the natural weighting regime, we find that the residual scaled standard clean follows incredibly well the Multi–Scale CLEAN results even at larger radii, which was not the case for the robust=0 case (see Fig. 2.3, bottom right panel). This is not an effect of the Multi–Scale CLEAN, but rather a consequence of the different sampling density in the centre of the uv plane for a natural weighted compared to a robust weighted map.

Regarding our final choice of α, since the LITTLE THINGS project is dealing with extended emission, we started on the premise that an α which is balancing out the time spent on the large scales and on the low scales would be most suited and as a result of our imaging tests we decided to use α = 0.2.

There are another two steering parameters, IMAGRPRM(13) and IMAGRPRM(14) which come in hand in the cases where the lower resolution fields become easily over cleaned. They allow the user to either lower the loops gain for a certain resolution (IMAGRPRM(13)), or weigh down the cut–off level in each major cycle for a certain resolution by a factor equal to IMAGRPRM(14). These two parameters have been used with their default values by the LITTLE THINGS team.

If we compare between Multi–Scale CLEAN and traditional imaging methods we find that the standard CLEAN has a peak flux density which is 40% higher than the Multi–Scale CLEAN or the residual scaled one (see Fig. 2.3, bottom left panel). This shows that Multi–Scale CLEAN, unlike standard CLEAN, properly addresses the wrong total flux problem. At the same time Multi–Scale CLEAN also deals with the missing short spacings better than the standard CLEAN, reducing considerably the negative bowl problem in extended sources.

We know that one can deal with the flux overestimation also by rescaling the map, a process in which the noise characteristics of the map are compromised (for more details, see Walter et al., 2008). This knowledge has prompted us to look into more detail at the noise characteristics of the Multi–Scale CLEAN and investigate whether this algorithm may be superior from this point of view as well. In Fig. 2.9 we present noise histograms for different choices of α corresponding to the cleaned maps and the 15″ and 45″ residual maps to show how the noise characteristics are being preserved to a major extent, meaning that when dealing with extended structure using Multi–Scale CLEAN leaves one with one final cube where the flux and noise characteristics are in no way seriously affected by the implementation of the applied algorithm.

For the LITTLE THINGS galaxies, we are combining data from three array configurations so we chose to work with 4 scales: 0 (innate resolution of the data), 15, 45 and 135 arcsecond resolution. We first determine the noise at each resolution by imaging a line–free channel. This value is further used in computing the cut–off level set with fgauss. For cut–offs, we use for each scale, a 2σ level for the robust cubes and a 2.5σ level for the natural cubes. We use IMAGRPRM(11)= 0.2 to ensure we are removing all the emission, which mostly is large scale structure. IMAGRPRM(11) works like a bias, it is steering the algorithm towards spending more time at the smaller scales when close to 1 and at larger scales when closer to 0. For all the 18 galaxies of my subsample, the mapping details of the natural and robust weighted data cubes are available in Table 2.4.

Once the two galaxies were imaged we put them through a by now standard blanking process (Walter et al., 2008), where we discriminate against any regions which do not show emission above a set level in at least three consecutive channels. Through this method we create a master blanking cube based on the smoothed to 25″ natural weighted maps blanked at 2σ or 2.5σ, which we further apply to all our cubes. Only then do we create the moment maps using the AIPS task XMOM. All moment maps used in this paper are primary beam corrected using task PBCOR.

Table 2.4. Map characteristics

Name	Weighting	Bmaj (″)	Bmin (″)	BPA (°)	Noise (mJy beam^{-1})	Size [pixels]	Pixel (″)	Chan.	Width (km s^{-1})
DDO 168	NA	12.6	11.2	63.2	0.47	1024	1.5	103	2.6
	RO	7.8	5.8	67.5	0.51				
DDO 133	NA	19.2	18.1	-84.0	0.33	1024	1.5	102	2.6
	RO	12.4	10.8	-87.9	0.37				
NGC 4214*	NA	14.7	13.9	-48.2	0.66	2048	1.5	108	1.3
	RO	7.6	6.4	89.8	0.73				
DDO 50*	NA	13.7	12.6	-40.1	1.02	2048	1.5	108	2.6
	RO	7.0	6.1	-32.9	1.07				
DDO 216	NA	20.0	18.9	55.2	0.88	1024	1.5	107	1.3
	RO	16.2	15.4	69.8	0.96				
NGC 2366*	NA	13.0	11.8	-1.6	0.61	1024	1.5	108	2.6
	RO	6.9	5.9	20.1	0.63				
WLM	NA	10.6	7.4	-14.2	0.76	1024	1.5	107	2.6
	RO	7.6	5.1	-3.4	0.82				
DDO187	NA	12.4	11.0	-88.8	0.54	1024	1.5	99	2.6
	RO	6.2	5.5	62.9	0.62				
DDO 155	NA	16.2	15.2	-52.9	0.60	1024	1.5	95	1.3
	RO	11.3	10.1	-84.6	0.65				
DDO 165	NA	14.8	12.9	78.1	0.62	1024	1.5	101	2.6

	RO	10.0	7.6	67.1	0.64				
IC1613	NA	13.2	11.0	-5.0	0.37	2048	1.5	107	2.6
	RO	7.7	6.5	6.7	0.40				
DDO 63*	NA	14.7	12.7	-41.6	1.06	1024	1.5	108	2.6
	RO	7.8	6.0	-71.5	1.19				
DDO 53*	NA	11.8	9.5	-6.0	0.56	1024	1.5	108	2.6
	RO	6.3	5.7	2.59	0.60				
DDO 75	NA	11.9	10.0	4.2	0.45	2048	1.5	104	2.6
	RO	7.6	6.5	13.7	0.51				
DDO 154*	NA	14.1	12.6	-58.1	0.52	1024	1.5	108	2.6
	RO	7.9	6.3	-87.2	0.54				
DDO 69	NA	8.3	7.7	70.8	0.62	1024	1.5	107	1.3
	RO	5.8	5.4	89.3	0.66				
M81dwA*	NA	15.9	14.2	10.2	0.74	1024	1.5	108	1.3
	RO	7.8	6.3	4.5	0.84				
DDO 210	NA	16.6	14.1	-4.0	0.80	1024	1.5	107	1.3
	RO	11.7	8.6	-6.78	0.87				

Table 2.4: From left to right the columns represent: Galaxy name, Weighting function used, Major axis of the synthesized beam in arcseconds, Minor axis of the synthesized beam in arcseconds, Position angle of the synthesized beam in degrees, Noise level in one channel map in mjy beam^{-1}, Size of the map in pixels, Pixel size in arcseconds, Number of channels, and Channel width in km s^{-1}. A star next to the galaxy name indicates the galaxies that are shared between the LITTLE THINGS and the THINGS projects. The galaxies in this table are ordered by metallicity.

2.4 Data Presentation

TBD

Here I want moment, maps, ancillary data maps. short text presenting the galaxies.

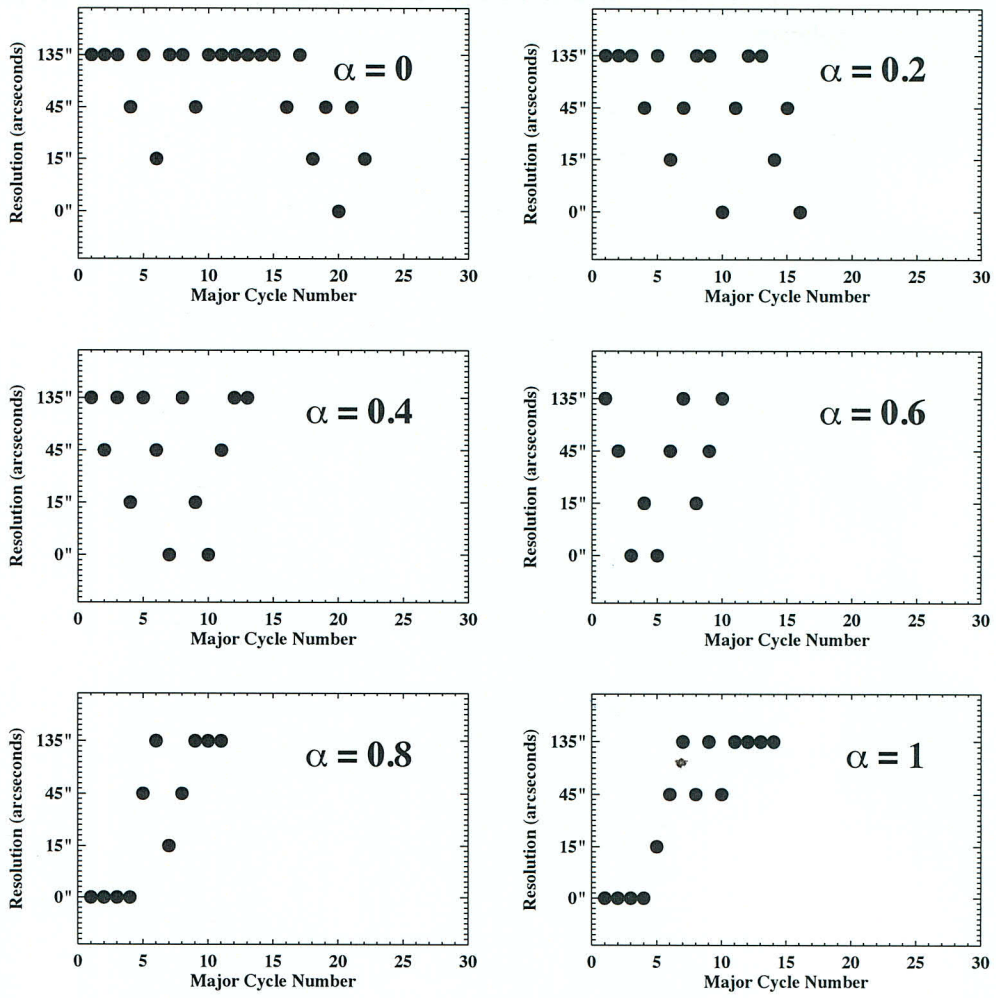

Figure 2.5: Testing the α parameter in DDO 168. Resolution scale versus major cycle number for α=0, 0.2, 0.4, 0.6, 0.8,1.0

Here + after —
give reader the take away point in the caption.